Chapter 6
Measurements of Airside Shear- and Wave-Induced Viscous Stresses over Strongly Forced Wind Waves

Kianoosh Yousefi, Fabrice Veron, and Marc P. Buckley

Abstract Detailed knowledge of the airflow over the surface of the ocean is paramount to evaluate and predict air-sea fluxes. The flux of momentum is of particular interest because it involves phenomena over a large spectrum of length and temporal scales from aerodynamic drag in large storm systems, down to the wind-wave generation problem at sub-centimeter scales. At the smaller scales, while there is a body of theoretical and experimental work which suggests that the wind-wave generation process is linked to the instability of the coupled air-water surface flow, progress has been hindered by the difficulties associated with making reliable measurements or simulations near the air-water interface at scales at which viscosity plays a role. In this paper, we present recent measurements of the two-dimensional velocity field in the turbulent airflow above wind waves. Improvements in measuring techniques have allowed us to detect the viscous sublayer in the airflow near the interface and make direct measurements of the airside viscous tangential stress (analogous to those made by (Banner ML, Peirson WL, J Fluid Mech 364:115–145, 1998) on the water side). Furthermore, we were able to separate mean, turbulent, and wave-coherent motions, and this decomposition yielded wave-coherent flow measurements as well as wave-phase averages of several flow field variables. We present the relationship of the varying surface viscous stress with the dominant wave phase. Also, to the authors' knowledge, we present the first measurements of airside wave-induced viscous stresses. We conclude that at low wind speed, surface viscous effects are substantial and likely need to be accounted for in the early stages of the wind-wave generation process.

K. Yousefi (✉)
Department of Mechanical Engineering, University of Delaware, Newark, DE, USA
School of Marine Science and Policy, University of Delaware, Newark, DE, USA
e-mail: kyousefi@udel.edu

F. Veron
School of Marine Science and Policy, University of Delaware, Newark, DE, USA
e-mail: fveron@udel.edu

M. P. Buckley
Institute of Coastal Research, Helmholtz-Zentrum Geesthacht, Geesthacht, Germany
e-mail: mbuckley@udel.edu

6.1 Introduction

The exchanges of momentum between the atmosphere and the ocean are strongly contingent on small-scale interfacial dynamics, particularly in low to moderate wind forcing conditions. These microphysical processes at the air-sea interface have important effects on the exchanges of momentum between the atmosphere and the ocean. However, relatively less attention has been paid to the tangential viscous stress and its contribution to the total air-sea momentum exchanges. This is in part because of the challenges associated with acquiring data close to the water surface (where viscosity is important) either in the open ocean or in the laboratory (Banner and Peirson 1998). In recent years, however, increased efforts have been made to examine the importance of viscous stress at the interface (e.g., Banner and Peirson 1998; Veron et al. 2007; Grare et al. 2013b; Peirson et al. 2014).

Several theoretical, numerical, and laboratory studies have investigated the tangential viscous stress over surface waves (e.g., Longuet-Higgins 1969; Okuda et al. 1977; Banner and Peirson 1998; Peirson and Banner 2003; Veron et al. 2007; Reul et al. 2008; Grare et al. 2013b; Peirson et al. 2014). These efforts were, in part, motivated by the need to better understand the early stages of the wave generation process. The early laboratory measurements of Okuda et al. (1977) estimated the shear stress at the air-sea interface from the aqueous boundary layer below water waves and concluded that the tangential stress predominantly supports the total wind stress for waves in strongly wind-forced conditions. In contrast, Banner and Peirson (1998) determined through a particle image velocimetry (PIV) technique at short fetches that the tangential stress does not contribute significantly to the total stress over very young wind-generated waves, though it is a non-zero fraction of the wind stress (see also Peirson 1997). Further works by Grare et al. (2013b) and Peirson et al. (2014) also determined that the contribution of the viscous stress to the total momentum flux is not negligible for low wind speeds but is possibly trivial at high wind speeds even close to the surface.

The airflow separation events over wind-driven waves significantly influence the distribution of the tangential viscous stress along the wave crest. The first studies measuring the viscous stress at the interface of surface waves in a laboratory, first performed by McLeish and Putland (1975) and Okuda et al. (1977) and furthered by Csanady (1985, 1990) and Kawamura and Toba (1988), qualitatively revealed that the tangential stress suddenly decreases to an almost zero value just past wave crests. Okuda et al. (1977) attributed the reduction of the viscous stress past the wave crest to the occurrence of airflow separation. More recently, Veron et al. (2007) also observed, through quantitative measurements of the velocity field on the airside of the water waves, that the tangential viscous stress is significantly reduced at the point of separation thereby leading to abrupt and dramatic along-wave variations in the viscous stress at the water surface (see also Reul et al. 2008). The tangential viscous stress increases again past the wave trough and reaches its peak value close to the wave crest.

As a general trend, the tangential stress over surface waves shows reductions compared to the flat or smooth water surfaces (Banner and Peirson 1998;

Kudryavtsev and Makin 2001). This can be partly explained by the fact that a portion of the total wind stress is carried by wave-coherent components when waves are present on the water surface. Moreover, the tangential viscous stress exhibits a phase-locked distribution over surface waves. Over both separating and non-separating wind waves, viscous stress presents a pattern of along-wave asymmetry close to the water interface in which it is highest (lowest) on the windward (leeward) side of waves (see Veron et al. 2007; Peirson et al. 2014). This is qualitatively consistent with predictions by Gent and Taylor (1976, 1977).

In recent years, there has been growing interest in evaluating the influences of the ocean surface waves on the turbulent flow structure above the water interface, and therefore, in the fundamental processes of wind-wave couplings. Although the primary features of the turbulent and wave-coherent momentum fluxes across the air-sea interface have received much attention over the last two decades (e.g., Hsu et al. 1981; Sullivan et al. 2000; Shen et al. 2003; Hara and Belcher 2004; Kihara et al. 2007; Yang and Shen 2010; Grare et al. 2013a; Hara and Sullivan 2015; Buckley and Veron 2016, 2019; Husain et al. 2019), the role of the tangential viscous stress in the air-sea momentum transfer is less well understood. In the current study, we present detailed measurements of the viscous stress within the viscous sublayer on the airside of the wind-driven surface waves and provide an estimation of its contribution to the total interfacial wind stress for low to strong wind forcing conditions. These measurements were acquired in the large wind-wave tunnel facility at the Air-Sea Interaction Laboratory of the University of Delaware using a combined PIV and laser-induced fluorescence (LIF) techniques (Buckley and Veron 2017). The paper is organized in the following fashion. In Sect. 6.2, the experimental setup and configurations are briefly described, along with the coordinate transformation and wave-turbulence decomposition. The results are discussed in Sect. 6.3 wherein the measurements of the mean and wave-induced tangential viscous stresses are presented in detail. Finally, a summary of the conclusions is offered in Sect. 6.4.

6.2   Experimental Configurations

6.2.1   Experimental Setup

The experimental measurements presented in the current study are based on the existing raw data obtained in the large wind-wave tunnel facility at the Air-Sea Interaction Laboratory of the University of Delaware (Buckley 2015; Buckley and Veron 2017). As schematically shown in Fig. 6.1, the wave tank has dimensions of 42 m length, 1 m width, and 1.25 m height of which 0.7 m filled with water to ensure sufficient airflow space above the water surface. A permeable absorbing beach was located at the end of the tank to dissipate the wave energy and eliminate the wave reflections. A honeycomb airflow straightener was also employed at the location of zero fetch to ensure uniform airflow across the tank and provide a smooth transition
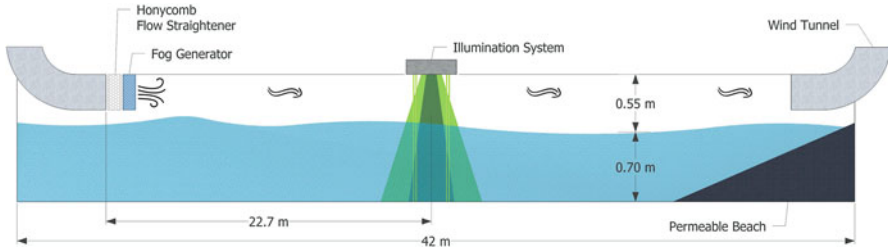
Fig. 6.1 Schematic representation of the large wind-wave tunnel facility at the Air-Sea Interaction Laboratory of the University of Delaware. The imaging data collection was located at a fetch of 22.7 m, and the airflow was seeded (fog particles) at the location of zero fetch. Airside velocity fields and wave properties were measured by PIV and LIF techniques, respectively. The flow is directed from left to right

from the wind tunnel inlet to the water surface. The flow visualization instruments were positioned at a fetch of 22.7 m. For the experiments presented here, various wind forcing conditions were considered with wind speeds ranging from 2.25 m s^{-1} to 16.59 m s^{-1}. The complete experimental conditions with corresponding wave properties are summarized in Table 6.1.

The quantitative velocity measurements were acquired using a combination of PIV and LIF techniques on the airside of surface wind waves within the viscous sublayer, on average, within 100 μm to the air-water interface. The PIV technique was employed to acquire along-channel two-dimensional airflow velocity fields above the wind waves. Water droplet particles (8–12 μm), used to seed the airflow, were illuminated with a high-intensity laser sheet and imaged by two adjacent digital cameras (Jai RM-4200, 2048 × 2048 pixels) at a frame rate of 14.4 fps. The two captured PIV frames were concatenated to produce a high-resolution 18.7 × 9.6 cm PIV image with a pixel resolution of 47 μm per pixel. An adaptive PIV algorithm similar to that described by Thomas et al. (2005) was applied to the concatenated PIV images, yielding a velocity vector measurement every 188 μm^2. Further, the LIF technique was utilized to accurately detect the surface profiles within the PIV field of view. To that end, high-resolution LIF images were simultaneously acquired with the PIV images using an identical digital camera (Jai RM-4200, 2048 × 2048 pixels) providing a high-resolution 20.48 × 20.48 cm image with a pixel resolution of 100 μm per pixel. In addition, large along-channel surface profiles of waves were obtained through the LIF technique and using a large field of view digital camera (Jai RM-4200, 2048 × 2048 pixel, 7.2 fps) equipped with a large field of view lens such that the final image spanned 51.20 × 51.20 cm with a resolution of 250 μm per pixel. An example of a raw large field of view (LFV) image along with the instantaneous horizontal velocity field estimated with the PIV is presented in Fig. 6.2. The reader is referred to Buckley (2015) and Buckley and Veron (2017) for the complete details of these experiments, including wind-wave facility, experimental setup, image acquisition, and processing procedures.

Table 6.1 Summary of experimental and flow conditions

U_{10} ($m\ s^{-1}$)	u_* ($m\ s^{-1}$)	C_p ($m\ s^{-1}$)	C_p/u_*	ζ_0 (mm)	δ_0 (mm)	a_p (cm)	k_p (m^{-1})	$\delta_0 k_p$	$a_p k_p$	f_p (Hz)
2.25	0.075	0.47	6.27	0.063	2.00	0.15	44.88	0.0876	0.07	3.3
5.08	0.168	0.62	3.69	0.056	0.89	0.50	25.13	0.0225	0.13	2.5
9.57	0.318	0.78	2.46	0.043	0.49	1.20	16.11	0.0079	0.19	2.0
14.82	0.567	0.87	1.53	0.290	0.26	1.96	13.09	0.0034	0.26	1.8
16.59	0.663	0.92	1.39	0.449	0.23	2.29	11.64	0.0026	0.27	1.7

The friction velocity, roughness height, and 10-m extrapolated velocity were calculated by fitting the logarithmic part of the mean wind velocity profile. The viscous sublayer thickness is estimated by $\delta_0 u_*/\nu = 10$ (Phillips 1977). The peak wave frequencies, f_p, obtained from frequency spectra of single point elevation measurements, and other parameters with subscript p derived by applying linear wave theory. The peak amplitude is $a_p = \sqrt{2} a_{rms}$ in which a_{rms} is the root-mean-square amplitude calculated from wave gauge time series.
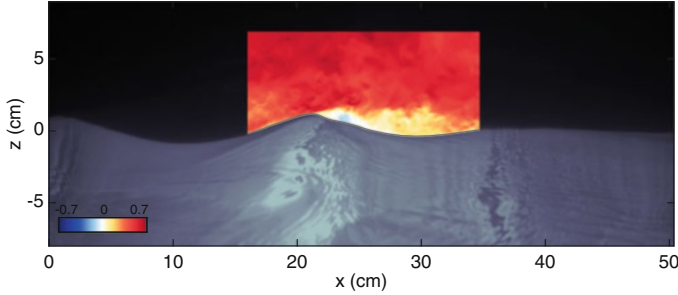
Fig. 6.2 Example of a raw large field of view (LFV) image plotted along with the measured instantaneous horizontal velocity field acquired with the PIV. The colorbar shows u/U_{10}, the horizontal velocity normalized with the 10-m equivalent wind speed; here U = 5.08 m s^{-1}

6.3 Coordinate Transformation and Triple Decomposition

In order to study the mean, wave, and turbulence contributions to the mean flow and air-sea momentum fluxes, it is necessary to separate mean, wave, and turbulent motions. Therefore, mean and phase averages need to be performed on the airside velocity field obtained experimentally, and to so requires a coordinate system that follows the wave motion, at least near the interface. By using surface elevation profiles $\eta(x)$ detected by the LIF camera, we were able to decompose the wave profiles within the PIV image into corresponding spatial Fourier components,

$$\eta(x) = \sum_n \eta_n = \sum_n a_n e^{i(k_n x + \varphi_n)} \tag{6.1}$$

where a_n, k_n, and φ_n are the amplitude, wavenumber, and phase of the nth mode in the Fourier decomposition of the surface $\eta(x)$, respectively. From there, it is relatively straightforward to derive a coordinate system that follows the water surface near the interface and tends toward a laboratory-attached Cartesian coordinate system far away from the surface. Thus, we define a wave-following coordinate system that relates to the Cartesian coordinates using the following expressions,

$$\xi(x, z) = x - i \sum_n \eta_n e^{-k_n \zeta}$$
$$\zeta(x, z) = z - \sum_n \eta_n e^{-k_n \zeta} \tag{6.2}$$

Here, lines of constant ζ are pseudo-horizontal in that $\zeta = 0$ gives $z = \eta(x)$, which is exactly the location of the wavy interface. Far from the influence of the waves (proportional here to the surface wave wavenumbers) lines of constant ζ tend toward Cartesian horizontal lines of constant z.

Accordingly, the ensemble mean velocity profiles $\bar{u}(\zeta)$ are obtained by simply averaging velocity profiles following these pseudo-horizontal ζ lines. Alternatively, by using the phase of the peak wave component (from the Fourier decomposition), each velocity profiles measured above the surface can be associated with the phase of the underlying wave, and phase-dependent velocity profiles $\langle u \rangle(\varphi, \zeta)$ can be obtained. Therefore, measured velocity fields can be decomposed into a phase-averaged component and a residual, which by definition is a turbulent component, i.e., $u(\xi, \zeta, t) = \langle u \rangle(\varphi, \zeta) + u'(\xi, \zeta, t)$. The phase-averaged velocity fields can be further decomposed into the mean and wave-induced components leading to the so-called triple decomposition of a velocity field (Hussain and Reynolds 1970),

$$u(\xi, \zeta, t) = \bar{u}(\zeta) + \tilde{u}(\varphi, \zeta) + u'(\xi, \zeta, t) \tag{6.3}$$

The general properties of the time and phase averages can be found in reports by Hussain and Reynolds (1970) and Reynolds and Hussain (1972).

6.4   Results

6.4.1   Governing Equations

In order to express the governing equations of fluid motion, we consider the Cartesian coordinate system in which (x, y, z) are respectively streamwise, spanwise, and vertical coordinates. The airflow is assumed to have a constant density and kinematic viscosity with the velocity components (u, v, w) in (x, y, z) directions, respectively. The equations of motion including continuity, momentum, and energy can be decomposed into the mean, wave-induced, and turbulent fluctuation components by applying the triple decomposition technique briefly described above. The starting point is substituting the decomposed variables into the governing equations, and then averaging; the time averaging is applied first and then the phase averaging. The mean, wave-induced, and turbulent momentum equations in a Cartesian coordinate system can be then expressed as,

$$\frac{\partial \bar{u}_i}{\partial t} + \frac{\partial}{\partial x_j}(\bar{u}_i \bar{u}_j) = -\frac{1}{\rho}\frac{\partial \bar{p}}{\partial x_i} + \frac{1}{\rho}\frac{\partial \bar{\tau}_{ij}}{\partial x_j} - \frac{\partial}{\partial x_j}(\overline{u'_i u'_j} + \overline{\tilde{u}_i \tilde{u}_j}) \tag{6.4}$$

$$\frac{\partial \tilde{u}_i}{\partial t} + \frac{\partial}{\partial x_j}(\bar{u}_i \tilde{u}_j) + \frac{\partial}{\partial x_j}(\tilde{u}_i \bar{u}_j) = -\frac{1}{\rho}\frac{\partial \tilde{p}}{\partial x_i} + \frac{1}{\rho}\frac{\partial \tilde{\tau}_{ij}}{\partial x_j} + \frac{\partial}{\partial x_j}(\overline{\tilde{u}_i \tilde{u}_j} - \tilde{u}_i \tilde{u}_j) - \frac{\partial \tilde{r}_{ij}}{\partial x_j} \tag{6.5}$$

$$\frac{\partial u_i'}{\partial t} + \frac{\partial}{\partial x_j}(u_i'\bar{u}_j) + \frac{\partial}{\partial x_j}(u_i'\tilde{u}_j) + \frac{\partial}{\partial x_j}(\bar{u}_i u_j') + \frac{\partial}{\partial x_j}(\tilde{u}_i u_j')$$

$$= -\frac{1}{\rho}\frac{\partial p'}{\partial x_i} + \frac{1}{\rho}\frac{\partial \tau_{ij}'}{\partial x_j} + \frac{\partial}{\partial x_j}(\langle u_i'u_j'\rangle - \overline{u_i'u_j'}) \qquad (6.6)$$

where $\tilde{r}_{ij} = \langle u_i'u_j'\rangle - \overline{u_i'u_j'}$ is the wave-induced turbulent stress, $-\overline{u_i'u_j'}$ is the Reynolds stress, and $-\overline{\tilde{u}_i\tilde{u}_j}$ is the wave-induced stress. Moreover, in these equations, the mean, wave-induced, and turbulent tangential viscous stresses can be respectively expressed as,

$$\bar{\tau}_{ij} = 2\mu\bar{S}_{ij} = \mu\left(\frac{\partial \bar{u}_i}{\partial x_j} + \frac{\partial \bar{u}_j}{\partial x_i}\right) \qquad (6.7)$$

$$\tilde{\tau}_{ij} = 2\mu\tilde{S}_{ij} = \mu\left(\frac{\partial \tilde{u}_i}{\partial x_j} + \frac{\partial \tilde{u}_j}{\partial x_i}\right) \qquad (6.8)$$

$$\tau_{ij}' = 2\mu S_{ij}' = \mu\left(\frac{\partial u_i'}{\partial x_j} + \frac{\partial u_j'}{\partial x_i}\right) \qquad (6.9)$$

where $\bar{S}_{ij}$, $\tilde{S}_{ij}$, and S_{ij}' are the mean, wave-induced, and turbulent strain rate tensors, respectively. In this paper, we are interested in examining the effects of wind waves on the tangential viscous stress terms. Specifically, the off-diagonal components of the viscous stress tensors are of importance in the turbulent boundary layer over surface waves.
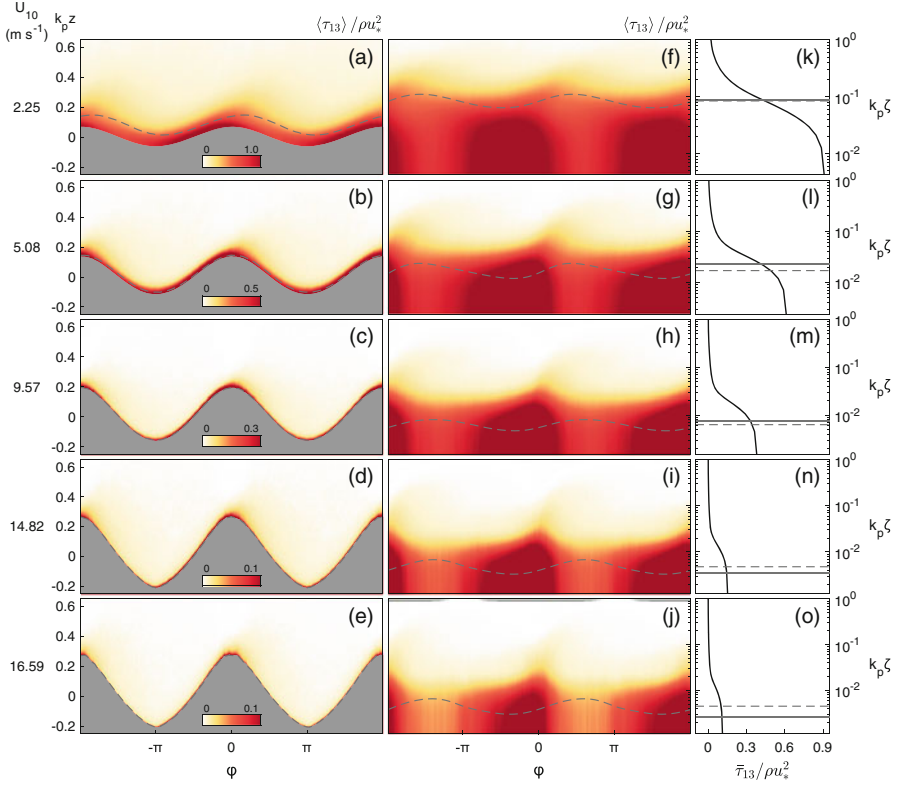
6.4.2 Mean Tangential Viscous Stress

The phase-averaged distribution of tangential viscous stress measurements normalized by the total wind stress is presented in Fig. 6.3 for experimental conditions with 10-m wind speeds varying from 2.25 m s^{-1} to 16.59 m s^{-1}. The right panels of Fig. 6.3 show the corresponding profiles of the mean tangential stress. The tangential viscous stress is computed from Eq. (6.7) for a two-dimensional flow field as,

$$\bar{\tau}_{13} = \mu\left(\frac{\partial \bar{u}}{\partial z} + \frac{\partial \bar{w}}{\partial x}\right) \qquad (6.10)$$

The surface waves are inducing a phase-locked variability in the viscous stress consistent with the results of, for example, Banner and Peirson (1998) and Veron et al. (2007). In general, the along wave distributions of the phase-averaged tangential viscous stress present an asymmetric pattern close to the surface; the viscous stress is intense upwind of wave crests with its maximum value about the wave crests, and less intense downwind of wave crests with its minimum in the middle of

Fig. 6.3 Phase-averaged distributions of the tangential viscous stress measurements (defined in Eq. 6.10) normalized with the total wind stress for all wind speed cases plotted on the (**a-e**) linear and (**f-j**) logarithmic scales. The corresponding vertical mean profiles of the tangential viscous stresses are also presented in the last column (panels **k-o**). The logarithmic phase-averaged and mean profile fields are plotted above the mean water surface as a function of dimensionless height $k_p\zeta$, while the linear vertical scale uses Cartesian coordinates $k_p z$. The dashed, grey lines indicate the location of the critical layer, i.e., the height at which $\langle u \rangle = C_p$, and the solid, grey lines indicate the height of the viscous sublayer. The 10-m wind speeds corresponding to each experimental condition are indicated on the left

the leeward side of waves. With increasing wind speed, the peak values of the normalized viscous stress reduce and shift downward. The magnitude of the peak viscous stress near the surface decreases from $\langle \tau_{13} \rangle / \tau = 1.20$ for $U_{10} = 2.25$ m s^{-1} to $\langle \tau_{13} \rangle / \tau = 0.19$ for $U_{10} = 16.59$ m s^{-1}, where $\tau = \rho u_*^2$ is the total wind stress. For the lowest wind speed, an enhanced viscous stress was observed at/near the water surface for almost the entire upwind face of the wave from $\varphi = -3\pi/4$ to $\varphi = 0$ in which the viscous stress was greater than the total stress. This is the region that the wave-coherent and turbulence are greatly suppressed. Close to the surface (at the height of $\zeta = 284$ μm), the normalized tangential viscous stress, averaged over the whole upwind side of the wave, is $\overline{(\langle \tau_{13} \rangle / \tau)}_{[-\pi,0]} = 1.05$, while it is

$\overline{(\langle \tau_{13} \rangle / \tau)}_{[0,\pi]} = 0.75$ averaged over the leeward side, for the wind speed of $U_{10} = 2.25$ m s^{-1}. We note that the phase-locked variations in tangential viscous stress exert important influences on the wave growth and the boundary layer thickness on the windward and leeward side of the waves. Finally, while the viscous stress is significant close to the surface, even for higher wind speed cases, it rapidly vanishes, as expected, farther from the interface outside of the viscous sublayer.

To further examine the near-surface viscous stresses, the mean tangential stress profiles are presented in the wall-layer coordinates in Fig. 6.4a on a logarithmic scale. The height of the critical layer is also indicated with cross symbols for each experimental case. As a general trend, the contribution of the viscous stress to the total momentum flux decreases with increasing wind speed consistent with the literature (e.g., Banner and Peirson 1998; Peirson et al. 2014). At the surface, however, the tangential viscous stress remains a considerable portion of the total wind stress, particularly at low to moderate wind forcing conditions. For the low wind speed of $U_{10} = 2.25$ m s^{-1}, the mean tangential viscous stress supports more than 90% of the total momentum flux at the interface and remains significant up to a dimensionless height of $\zeta^+ = 10$ with approximately a 40% contribution to the wind stress. Although the mean normalized tangential stress reduces with increasing wind speed, it still contributes more than 60% and 35% to the total stress for wind speeds of $U_{10} = 5.08$ m s^{-1} and $U_{10} = 9.57$ m s^{-1}, respectively. For strongly forced wind waves, the normalized mean viscous stress remains a non-zero portion of the total wind stress; it is approximately 15% and 11% of the total wind stress for the cases with $U_{10} = 14.82$ m s^{-1} and $U_{10} = 16.59$ m s^{-1}, respectively. Again, outside the
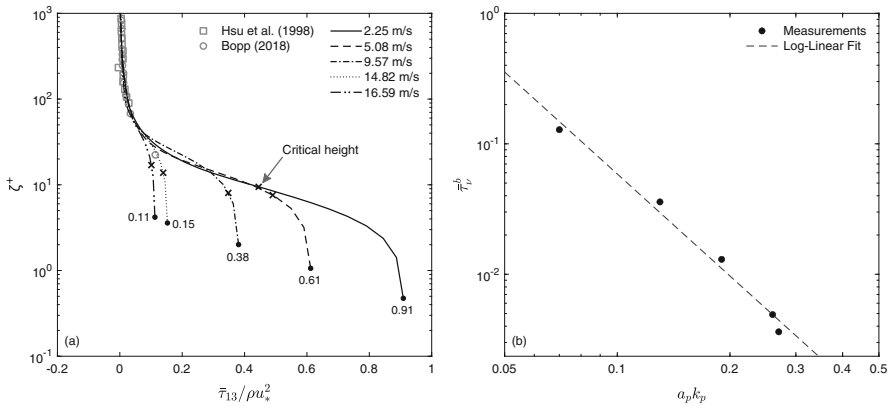
Fig. 6.4 (a) Vertical profiles of the mean tangential viscous stress (defined in Eq. 6.10) normalized by the total wind stress for different experimental conditions plotted as a function of dimensionless law-of-the-wall height, i.e., $\zeta^+ = \zeta u_*/\nu$, on the logarithmic scale. The results of Hsu et al. (1981) for mechanically generated water waves with $U_{10} = 2.4$ m s^{-1} and $C_p/u_* = 18.2$ and Bopp (2018) for wind waves with $U_{10} = 12$ m s^{-1} and $C_p/u_* = 1.7$ are also indicated by square and circle symbols, respectively, for comparison purposes. The location of the critical layer is also denoted by cross symbols. (b) Height-integrated tangential viscous stress $\bar{\tau}_\nu^b$ (defined in Eq. 6.11) as a function of wave slope. The dashed line is the best fit through the data and shows $\bar{\tau}_\nu^b \propto (a_p k_p)^{-2.6}$

viscous sublayer farther above the surface, the viscous stress rapidly drops to zero, and consequently, the influences of viscosity become trivial.

The normalized tangential viscous stress profiles integrated within the wave boundary layer (i.e., up to $\zeta = k_p$) are defined as,

$$\bar{\tau}_\nu^b = \frac{k_p}{\rho u_*^2} \int_0^1 |\bar{\tau}_{13}| \, d\zeta \qquad (6.11)$$

and displayed in Fig. 6.4b as a function of wave slope. They represent the average contribution of the viscous stress to the wind stress. As expected, the height-integrated contribution of the viscous stress decreases with the wave slope (or equivalently in these single fetch experiments, with the 10-m wind speed).

6.4.3   Wave-Induced Tangential Viscous Stress

In this section, we investigate the wave-induced tangential viscous stress in the wave boundary layer. The wave-induced tangential viscous stress, for these two-dimensional experimental data, can be estimated using Eq. (6.8) and reduces to,

$$\tilde{\tau}_{13} = \mu \left(\frac{\partial \tilde{u}}{\partial z} + \frac{\partial \tilde{w}}{\partial x} \right) \qquad (6.12)$$

In Fig. 6.5, we first present the phase-averaged distributions of wave-induced viscous stress. The streamwise-averaged (average across all phases) profiles of the absolute value of $\tilde{\tau}_{13}$ fields, i.e., $\overline{|\tilde{\tau}_{13}|}$ where $|\tilde{\tau}_{13}|$ is the absolute value, are also plotted on the right panels (k-o). All the terms are normalized by the total wind stress. Over the lowest wind speed, the wave-induced tangential stress was positive (negative) upwind (downwind) side of wave crests below the critical height with its positive and negative peaks located about the middle of the windward and leeward face of the waves (see Fig. 6.5 panels a and f). Above the critical height, this positive-negative pattern in the wave viscous stress was substantially shifted in the downstream direction by almost $3\pi/4$. In high winds, the pattern of positive-negative asymmetry in the wave-induced tangential stress can also be observed very close to the interface (see Fig. 6.5 panels b-e and g-j). With increasing wind speed, the region of positive wave-induced viscous stress on the windward side of waves moves downwind, while the negative stress on the leeward side of waves slightly extends up to the windward face of the next wave. The location of extrema in the wave viscous stress also moves downwind with increasing wind speed. The positive extremum was located at a phase of approximately $-85°$, $-60°$, $-30°$, $-25°$ for the wind speeds of $U_{10} = 2.25$ m s^{-1}, $U_{10} = 5.08$ m s^{-1}, $U_{10} = 9.57$ m s^{-1}, and $U_{10} = 14.82$ m s^{-1}, respectively. The negative extremum was also shifted from a phase of $95°$ for $U_{10} = 5.08$ m s^{-1} to a phase of about $115°$ for $U_{10} = 16.59$ m s^{-1}.
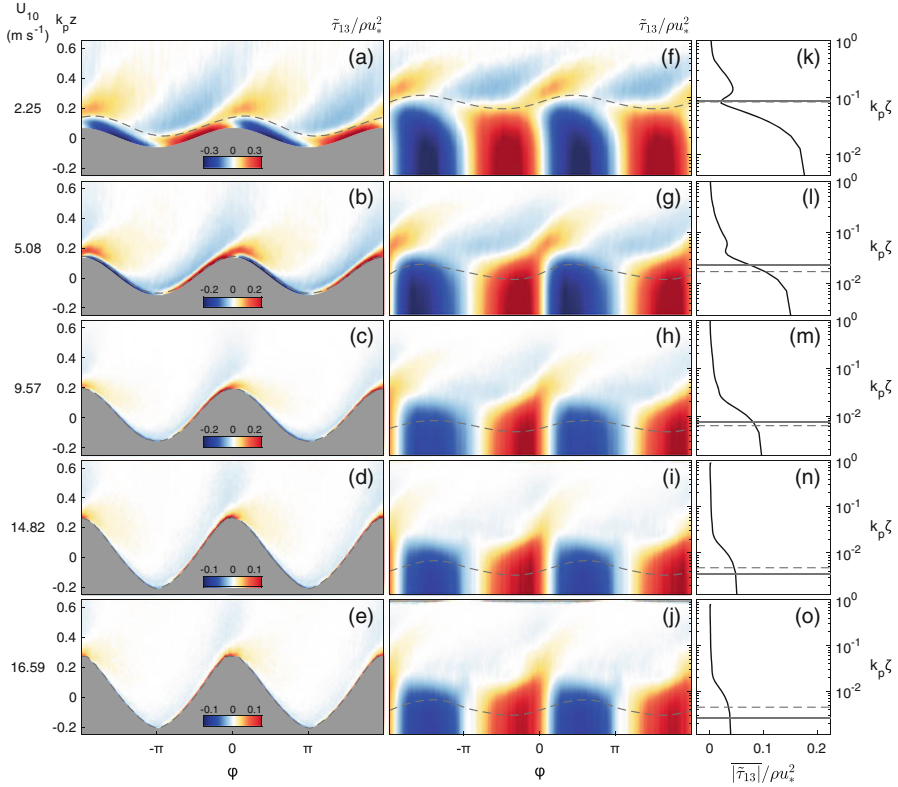
Fig. 6.5 Phase-averaged distributions of the wave-induced tangential viscous stress (see Eq. 6.12) for all wind-wave experiments plotted on the (**a–e**) linear and (**f–j**) logarithmic scales. The corresponding streamwise-averaged profiles of the absolute value of $\tilde{\tau}_{13}$ fields, i.e., $\overline{|\tilde{\tau}_{13}|}$ where $|\tilde{\tau}_{13}|$ is the absolute value, are also presented on the right panels (**k-o**). All fields are normalized by the total wind stress, i.e., ρu_*^2. The logarithmic phase-averaged and streamwise-averaged fields are plotted above the mean water surface as a function of dimensionless height $k_p\zeta$, while the linear vertical scale uses Cartesian coordinates $k_p z$. The dashed and solid lines denote the location of the critical layer and viscous sublayer, respectively. The 10-m wind speeds corresponding to each experimental case are indicated on the left

At the lowest wind speed, however, the negative peak was positioned closer to the wave trough at a phase of approximately 110°. Moreover, farther above the surface, the wave viscous stress forms a negative-positive pattern along the wave crest. In general, the wave-induced viscous stress quickly reduces away from the surface. To the author's knowledge, these are the first measurements of airside wave-induced viscous stresses.

The streamwise-averaged profiles of wave-induced tangential viscous stress are also shown in Fig. 6.5 panels k-o. As expected, the variations of $\overline{|\tilde{\tau}_{13}|}$ are mainly constrained in the vicinity of the water surface and rapidly tends toward zero farther above the surface. The magnitude of streamwise-averaged wave viscous

stress decreases as the wind speed increases, which is consistent with the behavior of the mean viscous stress. In general, the wave-induced viscous stresses are smaller than the mean tangential viscous stresses by almost an order of magnitude but still can be, on average, 10% of the total wind stress for low to moderate wind forcing conditions. The wave-induced tangential viscous stress supports about 17%, 10%, and 7% of the total wind stress for wind speeds of 2.25 m s^{-1}, 5.08 m s^{-1}, and 9.57 m s^{-1}, respectively. It is, however, trivial for higher wind speeds. The wave-induced tangential viscous stress, in fact, represents viscous forces due to the wave motion and equals the rate of momentum loss of waves through the viscosity.

The streamwise-averaged profiles of wave-induced viscous stresses are next plotted in Fig. 6.6a as a function of dimensionless wave viscous layer height, i.e., $\zeta^{\omega} = \zeta\sqrt{\omega/\nu}$, on a logarithmic scale as we are interested in small scale processes very close to the water interface. Here, all the profiles are appropriately normalized by the orbital velocities $\rho(a\omega)^2$ where ω is the angular frequency and $\omega^2 = gk$ is the dispersion relationship for propagating deep water waves. It can be observed that the (streamwise-averaged) wave tangential stress decreases with wind speed; it was $\overline{|\tilde{\tau}_{13}|}/\rho(a\omega)^2 = 1.03$ for wind speed of $U_{10} = 2.25$ m s^{-1} and reduced to approximately $\overline{|\tilde{\tau}_{13}|}/\rho(a\omega)^2 = 0.3$ for the wind speed of $U_{10} = 16.59$ m s^{-1}. The wave-induced viscous stress remains significant up to a height of about $\zeta^{\omega} = 1$ for all experimental conditions, even the highest wind speed cases, and then falls to zero farther outside the wave viscous layer. As for the viscous tangential stress, close to the surface, the streamwise-averaged wave tangential stresses are nearly constant, showing a constant behavior in the wave
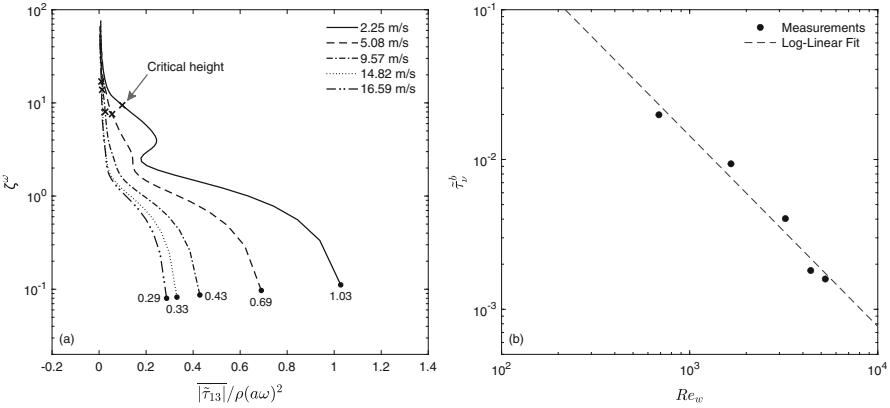

Fig. 6.6 (**a**) Vertical profiles of the streamwise-averaged wave-induced viscous stress, i.e., $\overline{|\tilde{\tau}_{13}|}$ where $|\tilde{\tau}_{13}|$ is the absolute value, plotted against the height of the wave viscous, i.e., $\zeta^{\omega} = \zeta\sqrt{\omega/\nu}$, on a logarithmic scale for all wind speed cases. Note that these stress profiles are normalized by $\rho(a\omega)^2$. The cross symbols are the height of the critical layer. (**b**) Height-integrated wave-induced viscous stress $\tilde{\tau}_{\nu}^b$ (defined in Eq. 6.13) as a function of wave Reynolds number, i.e., $Re_w = \omega/\nu k^2$. The dashed line shows $\tilde{\tau}_{\nu}^b \propto (Re_w)^{-1.3}$ (or $\tilde{\tau}_{\nu}^b \propto (a_p k_p)^{-1.85}$)

boundary layer. This is somewhat unexpected since, in theory, there should be some weak shear in the wave-coherent velocity fields near the interface. The height-integrated of the streamwise-averaged wave-induced viscous stress profiles (i.e., bulk representation) are also defined as,

$$\tilde{\tau}_\nu^b = \frac{k_p}{\rho u_*^2} \int_0^1 \overline{|\tilde{\tau}_{13}|} \, d\zeta \tag{6.13}$$

and shown in Fig. 6.6b against the wave Reynolds number $Re_w = \omega/\nu k^2$. The height-integrated wave-induced viscous stress represents the average contribution of the wave-induced viscous stress to the total wind stress. The height-integrated contribution of wave-induced viscous stress decreases with the wave Reynolds number, or equivalently, wind speed. This observed trend is consistent with the variations of the height-integrated tangential viscous stress (see Fig. 6.4b).

Finally, in Fig. 6.7, we show along-wave surface distributions of the wave-induced viscous stress for all experimental conditions. These near-surface data were calculated by taking averages within the viscous sublayer and normalized by
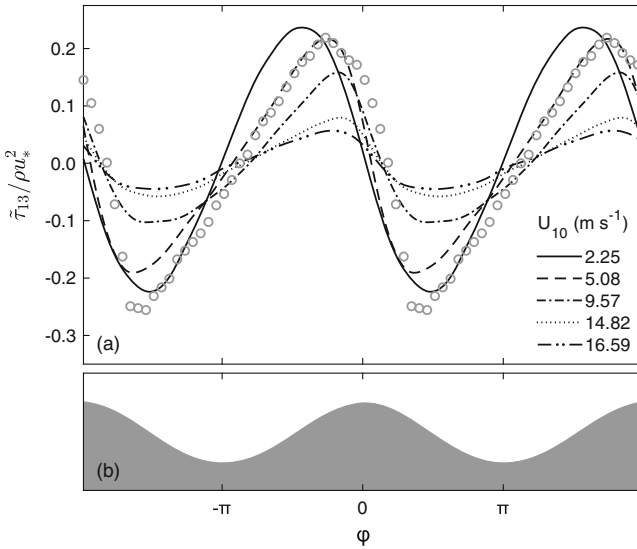
Fig. 6.7 (**a**) Along-wave surface profiles of the wave-induced viscous stress (whiten the viscous sublayer) normalized by the total wind stress ρu_*^2 for all experimental conditions. The results of Banner and Peirson (1998), which is for $U_{10} = 12.8$ m s^{-1} and fetch of 4.35 m, are also shown by circle symbols for comparison. It should be noted here that no reliable data could be collected by Banner and Peirson (1998) for some locations along the leeward side of the waves such as the spilling regions and trough regions, and thus, the data are interpolated for the leeward side of the waves. The bottom of the figure (*panel b*) shows a sketch of the mean wave profile to visualize the wave phase

the total wind stress. For comparison, the data from Banner and Peirson (1998) for $U_{10} = 12.8$ m s^{-1} at a fetch of 4.35 m are also shown with grey circles. The wave-induced viscous stress is compiled from Banner and Peirson (1998) data by subtracting the mean tangential stress from phase-averaged fields, so that $\tilde{\tau}_{13} = \langle \tau_{13} \rangle - \bar{\tau}_{13}$. It should be noted here that no reliable data could be collected by Banner and Peirson (1998) for locations along the leeward side of the waves such as the spilling and trough regions, and thus, they interpolated their data for the leeward side of the waves. It can be observed from Fig. 6.7 that the wave-induced tangential stresses, on average, exhibits important along-wave variations in all wind forcing conditions. In all cases, the wave-induced tangential stress data indicate a peak upwind of the wave crest ($\varphi \sim -\pi/4$) and a dip at approximately the middle of the leeward face of waves ($\varphi \sim \pi/2$). This is in complete agreement with the measurements of Banner and Peirson (1998) for microscale breaking wind waves. As wind speed increases, the peak value of the normalized wave viscous stress decreases from 0.24 for $U_{10} = 2.25$ m s^{-1} to 0.06 for $U_{10} = 16.59$ m s^{-1}, while the minimum value increases from -0.22 for $U_{10} = 2.25$ m s^{-1} to -0.04 for $U_{10} = 16.59$ m s^{-1}.

6.5 Conclusions

In this paper, we presented high-resolution viscous tangential measurements in the airflow above wind-generated surface waves within the viscous sublayer for different wind-wave conditions at a fetch of 22.7 m and with a range of 10-m wind speed varying from 2.25 to 16.59 m s^{-1}. To this end, two-dimensional velocity fields in the turbulent airflow above the waves were acquired in the laboratory using a combination of PIV and LIF techniques. Upon separating the mean, wave-coherent, and turbulence motions, we were further able to examine the mean and wave phase-coherent tangential viscous stress fields separately.

The surface waves are inducing a phase-locked variability in the viscous stress. As a general trend, the phase-averaged distribution of the viscous stress forms a pattern of along-wave asymmetry near the surface; it is highest on the upwind face of wave crest with its peak value close to the wave crest and its minimum about the middle of the leeward side of waves. Although the contribution of the viscous stress to the total momentum flux decreases with increasing wind speed, it is not negligible for low to moderate wind speeds. Close to the water interface, the mean tangential stress supported more than 90% of the wind stress for the low wind speed of $U_{10} = 2.25$ m s^{-1} and remained considerable up to a dimensionless height of $\zeta^+ = 10$ with approximately a 40% contribution to the total wind stress. With increasing wind speed, the surface contribution, however, reduced (exponentially) to almost 60% and 35% of the total stress for wind speeds of $U_{10} = 5.08$ m s^{-1} and $U_{10} = 9.57$ m s^{-1}, respectively. The viscous stress is always a non-zero fraction of the total momentum flux, even for strong wind forcing conditions.

Close to the surface, the phase-averaged distributions of the wave-induced tangential stress are positive (negative) upwind (downwind) side of wave crests below the critical height with their positive and negative extrema located about the middle of the windward and leeward face of the waves. Farther above the surface, this positive-negative pattern in the wave viscous stress is substantially shifted in the downstream direction above the critical height. Moreover, the wave-induced viscous stress quickly reduces to a zero value away from the surface. The streamwise-averaged profiles of wave-induced tangential stress are also shown to be mainly constrained in the vicinity of the water surface, and consistent with the mean viscous stress, their magnitude decreases as wind speed increases. In general, the wave-induced viscous stresses are smaller than the mean viscous stresses by almost an order of magnitude, but still can be on average 10% of the total wind stress for low to moderate wind speeds; it was about 17%, 10%, and 7% of the total wind stress for wind speeds of $U_{10} = 2.25$ m s^{-1}, $U_{10} = 5.08$ m s^{-1}, and $U_{10} = 9.57$ m s^{-1}, respectively.

Overall, mean tangential and wave-coherent viscous stresses carry a substantial fraction of the total air-sea stress, particularly at low wind speeds. Thus, we postulate that the viscous tangential stress in the airflow at the interface is likely to be an integral part of the wave generation process, but detailed experiments, simulations, and theoretical investigations of the early stages of the wind-wave generation mechanisms are still needed.

References

Banner, M. L., & Peirson, W. L. (1998). Tangential stress beneath wind-driven air-water interfaces. *Journal of Fluid Mechanics, 364*, 115–145.

Bopp, M. (2018). *Air-flow and stress partitioning over wind waves in a linear wind-wave facility* (Doctoral dissertation), Heidelberg: Heidelberg University.

Buckley, M. P., (2015). *Structure of the airflow above surface waves*. (Doctoral dissertation), Newark: University of Delaware.

Buckley, M. P., & Veron, F. (2016). Structure of the airflow above surface waves. *Journal of Physical Oceanography, 46*(5), 1377–1397.

Buckley, M. P., & Veron, F. (2017). Airflow measurements at a wavy air–water interface using PIV and LIF. *Experiments in Fluids, 58*(11), 161.

Buckley, M. P., & Veron, F. (2019). The turbulent airflow over wind generated surface waves. *European Journal of Mechanics - B/Fluids, 73*, 132–143.

Csanady, G. (1985). Air-sea momentum transfer by means of short-crested wavelets. *Journal of Physical Oceanography, 15*(11), 1486–1501.

Csanady, G. (1990). Momentum flux in breaking wavelets. *Journal of Geophysical Research: Oceans, 95*(C8), 13289–13299.

Gent, P. R., & Taylor, P. A. (1976). A numerical model of the air flow above water waves. *Journal of Fluid Mechanics, 77*, 105–128.

Gent, P. R., & Taylor, P. A. (1977). A note on separation over short wind waves. *Boundary-Layer Meteorology, 11*(1), 65–87.

Grare, L., Lenain, L., & Melville, W. K. (2013a). Wave-coherent airflow and critical layers over ocean waves. *Journal of Physical Oceanography, 43*(10), 2156–2172.

Grare, L., Peirson, W. L., Branger, H., Walker, J. W., Giovanangeli, J. P., & Makin, V. (2013b). Growth and dissipation of wind-forced, deep-water waves. *Journal of Fluid Mechanics, 722*, 5–50.

Hara, T., & Belcher, S. E. (2004). Wind profile and drag coefficient over mature ocean surface wave spectra. *Journal of Physical Oceanography, 34*(11), 2345–2358.

Hara, T., & Sullivan, P. P. (2015). Wave boundary layer turbulence over surface waves in a strongly forced condition. *Journal of Physical Oceanography, 45*(3), 868–883.

Hsu, C. T., Hsu, E. Y., & Street, R. L. (1981). On the structure of turbulent flow over a progressive water wave: Theory and experiment in a transformed, wave-following coordinate system. *Journal of Fluid Mechanics, 105*, 87–117.

Hussain, A. K. M. F., & Reynolds, W. C. (1970). The mechanics of an organized wave in turbulent shear flow. *Journal of Fluid Mechanics, 41*, 241–258.

Husain, N. T., Hara, T., Buckley, M. P., Yousefi, K., Veron, F., & Sullivan, P. P. (2019). Boundary layer turbulence over surface waves in a strongly forced condition: LES and observation. *Journal of Physical Oceanography, 49*(8), 1997–2015.

Kawamura, H., & Toba, Y. (1988). Ordered motion in the turbulent boundary layer over wind waves. *Journal of Fluid Mechanics, 197*, 105–138.

Kihara, N., Hanazaki, H., Mizuya, T., & Ueda, H. (2007). Relationship between airflow at the critical height and momentum transfer to the traveling waves. *Physics of Fluids, 19*(1), 015102.

Kudryavtsev, V. N., & Makin, V. K. (2001). The impact of air-flow separation on the drag of the sea surface. *Boundary-Layer Meteorology, 98*(1), 155–171.

Longuet-Higgins, M. S. (1969). Action of a variable stress at the surface of water waves. *Physics of Fluids, 12*(4), 737–740.

McLeish, W., & Putland, G. E. (1975). Measurements of wind-driven flow profiles in the top millimeter of water. *Journal of Physical Oceanography, 5*(3), 516–518.

Okuda, K., Kawai, S., & Toba, Y. (1977). Measurement of skin friction distribution along the surface of wind waves. *Journal of Oceanography, 33*(4), 190–198.

Peirson, W. L. (1997). Measurement of surface velocities and shears at a wavy air–water interface using particle image velocimetry. *Experiments in Fluids, 23*(5), 427–437.

Peirson, W. L., & Banner, M. L. (2003). Aqueous surface layer flows induced by microscale breaking wind waves. *Journal of Fluid Mechanics, 479*, 1–38.

Peirson, W. L., Walker, J. W., & Banner, M. L. (2014). On the microphysical behavior of wind-forced water surfaces and consequent re-aeration. *Journal of Fluid Mechanics., 743*, 399–447.

Phillips, O. M. (1977). *The dynamics of the upper ocean* (2nd ed.). Cambridge/London/New York/Melbourne: Cambridge University Press.

Reul, N., Branger, H., & Giovanangeli, J. P. (2008). Air flow structure over short-gravity breaking water waves. *Boundary-Layer Meteorology, 126*(3), 477–505.

Reynolds, W. C., & Hussain, A. K. M. F. (1972). The mechanics of an organized wave in turbulent shear flow. Part 3. Theoretical models and comparisons with experiments. *Journal of Fluid Mechanics, 54*, 263–288.

Shen, L., Zhang, X., Yue, D. K. P., & Triantafyllou, M. S. (2003). Turbulent flow over a flexible wall undergoing a streamwise travelling wave motion. *Journal of Fluid Mechanics, 484*, 197–221.

Sullivan, P. P., McWilliams, J. C., & Moeng, C. H. (2000). Simulation of turbulent flow over idealized water waves. *Journal of Fluid Mechanics, 404*, 47–85.

Thomas, M., Misra, S., Kambhamettu, C., & Kirby, J. T. (2005). A robust motion estimation algorithm for PIV. *Measurement Science and Technology, 16*(3), 865.

Veron, F., Saxena, G., & Misra, S. K. (2007). Measurements of the viscous tangential stress in the airflow above wind waves. *Geophysical Research Letters, 34*(19), L19603.

Yang, D. I., & Shen, L. (2010). Direct-simulation-based study of turbulent flow over various waving boundaries. *Journal of Fluid Mechanics, 650*, 131–180.